

# Electrocatalytic reduction of NO to NH<sub>3</sub> in ionic liquids by P-doped TiO<sub>2</sub> nanotubes

Shangcong Zhang<sup>1,2</sup>, Qian Liu<sup>3</sup>, Xinyue Tang<sup>4</sup>, Zhiming Zhou<sup>4</sup>, Tiejian Fan<sup>4</sup>, Yingmin You (✉)<sup>1,2</sup>,  
Qingcheng Zhang (✉)<sup>4</sup>, Shusheng Zhang<sup>5</sup>, Jun Luo<sup>6</sup>, Xijun Liu (✉)<sup>7</sup>

<sup>1</sup> College of Electrical and Electronic Engineering, Wenzhou University, Wenzhou 325035, China

<sup>2</sup> Low Voltage Apparatus Technology Research Centre of Zhejiang, Wenzhou University, Wenzhou 325035, China

<sup>3</sup> Institute for Advanced Study, Chengdu University, Chengdu 610106, China

<sup>4</sup> College of Chemistry and Materials Engineering, Wenzhou University, Wenzhou 325035, China

<sup>5</sup> College of Chemistry, Zhengzhou University, Zhengzhou 450000, China

<sup>6</sup> Tianjin Key Lab for Photoelectric Materials & Devices, School of Materials Science and Engineering, Tianjin University of Technology, Tianjin 300384, China

<sup>7</sup> State Key Laboratory of Featured Metal Materials and Life-cycle Safety for Composite Structures, School of Resource, Environments and Materials, Guangxi University, Nanning 530004, China

© Higher Education Press 2023

**Abstract** Designing advanced and cost-effective electrocatalytic system for nitric oxide (NO) reduction reaction (NORR) is vital for sustainable NH<sub>3</sub> production and NO removal, yet it is a challenging task. Herein, it is shown that phosphorus (P)-doped titania (TiO<sub>2</sub>) nanotubes can be adopted as highly efficient catalyst for NORR. The catalyst demonstrates impressive performance in ionic liquid (IL)-based electrolyte with a remarkable high Faradaic efficiency of 89% and NH<sub>3</sub> yield rate of 425 μg·h<sup>-1</sup>·mg<sub>cat.</sub><sup>-1</sup>, being close to the best-reported results. Noteworthy, the obtained performance metrics are significantly larger than those for N<sub>2</sub> reduction reaction. It also shows good durability with negligible activity decay even after 10 cycles. Theoretical simulations reveal that the introduction of P dopants tunes the electronic structure of Ti active sites, thereby enhancing the NO adsorption and facilitating the desorption of \*NH<sub>3</sub>. Moreover, the utilization of IL further suppresses the competitive hydrogen evolution reaction. This study highlights the advantage of the catalyst–electrolyte engineering strategy for producing NH<sub>3</sub> at a high efficiency and rate.

**Keywords** nitric oxide reduction reaction, electrocatalysis, ammonia production, phosphorus-doped titania

## 1 Introduction

Ammonia (NH<sub>3</sub>) is one of the most highly important artificial chemicals used in the industry that can act as an essential precursor for nitrogen fertilizers, medicine production, dyes, and so on. In contrast, nitric oxide (NO) is a primary air pollutant of great concern as it is directly related to many diseases and malfunctions [1–5]. In general, the fixation of molecular nitrogen (N<sub>2</sub>) to NH<sub>3</sub> is a key step for the natural N<sub>2</sub> cycle [6–10]. However, the strong and nonpolar N≡N bond makes the N<sub>2</sub> molecule extremely stable and inert [11,12]. Accordingly, the industrial Haber–Bosch process requires a large amount of energy input and involves the emission of greenhouse gases as well [13,14]. In contrast, electrosynthesis powered by renewable electricity represents a promising approach for producing NH<sub>3</sub> under ambient conditions and thus attracts significant research attention, in particular, for N<sub>2</sub> reduction reaction (NRR) [15–17]. However, the reported NH<sub>3</sub> yield rate and Faradaic efficiency (FE) are obviously far away from the industrial requirements [18]. Therefore, development of more efficient electrocatalytic system toward NH<sub>3</sub> production is highly desirable and demands systematic explorations.

Recently, some advances have been achieved in electrochemical denitration (that is, NO reduction reaction (NORR)) [11,12,19]; and metal [11], alloy [20], and sulfide [21] have been reported as potential NORR-active materials. Theoretically, NO exhibits lower cleavage energy and better solubility compared to N<sub>2</sub>, which is expected to be beneficial for more efficient

Received September 16, 2022; accepted October 16, 2022

E-mails: yymfd@163.com (You Y.), zhangqc@wzu.edu.cn (Zhang Q.), xjliu@tjut.edu.cn (Liu X.)

electrosynthesis of  $\text{NH}_3$ . For example, Peng et al. [12] used single niobium (Nb) atoms as superior NORR electrocatalyst under ambient conditions. Sun and coworkers [21] confirmed that  $\text{MoS}_2$  nanosheets could display a high  $\text{NH}_3$  yield rate of  $281.1 \mu\text{g}\cdot\text{h}^{-1}\cdot\text{mg}_{\text{cat}}^{-1}$  in acidic media. Noteworthy, the selective catalytic reduction technology has been widely adopted for NO abatement, which consumes massive  $\text{NH}_3$  and  $\text{H}_2$  [11,12]. In this case, NORR offers an appealing strategy for NO removal. Although the related improvements have been made, desirable NORR performance while largely suppressing competitive hydrogen evolution reaction (HER, in particular, at more negative potentials) has still not been achieved. In this regard, heteroatom doping has been regarded as an effective strategy to optimize electrochemical performance [6,22–24]. Besides, electrolytes can also significantly affect the interfacial properties, and directly impact catalyst selectivity and overall activity [25,26]. Keeping these considerations in mind, herein it is inferred that the combination of catalyst-doping and electrolyte-optimization may be a feasible strategy to promote NORR.

In this study, phosphorus (P)-doped titania ( $\text{TiO}_2$ ) nanotubes (P-TNTs) were synthesized via a two-step approach. Further, it was found that these nanotubes exhibited a notably high NO-to- $\text{NH}_3$  conversion with a maximum  $FE_{\text{NH}_3}$  of 89% and a corresponding yield rate of  $425 \mu\text{g}\cdot\text{h}^{-1}\cdot\text{mg}_{\text{cat}}^{-1}$  in an ionic liquid (IL)-containing electrolyte. Moreover, these nanotubes also exhibited impressive NORR durability over 10 cycles. The obtained performance metrics were found to be comparable to the best-reported results (see details in Table S1 (cf. Electronic Supplementary Material, ESM)). Density functional theory (DFT) was further used to verify that the introduction of P dopants could activate NO molecule and simultaneously accelerated the desorption of  $^*\text{NH}_3$ . Moreover, the usage of hydrophobic IL was able to effectively suppress the competitive HER. Accordingly, the catalyst-electrolyte engineering offers a novel strategy for the development of high-performance NORR catalysts as well as for other electrochemical reactions.

## 2 Experimental

### 2.1 Synthesis and characterizations

Preparation of P-TNTs and TNTs. Preparation was carried out following the literature method [27], briefly,  $\text{TiO}_2$  powder (3 g) was added to NaOH solution (50 mL,  $10 \text{ mol}\cdot\text{L}^{-1}$ ) in a polytetrafluoroethylene (PTFE, Teflon) beaker under vigorous stirring. The solution was placed in a PTFE-lined autoclave and heated for 22 h at a controlled temperature in the range 120–160 °C. The white, powdery TNTs were thoroughly washed with

water until the washing solution achieved pH 7. The obtained TNTs were heat treated at 400 °C for 2 h in a crucible in the presence of  $\text{NaH}_2\text{PO}_2$ . The reference sample (TNTs) was prepared via an identical synthesis route but without  $\text{NaH}_2\text{PO}_2$  addition. Notably, all the chemicals were of analytical grade and were purchased from Sigma-Aldrich. The NaOH solution used in this study was prepared using ultrapure water ( $18.2 \text{ M}\Omega$ ) from Millipore purification system. Further, inductively coupled plasma spectrometry measurements excluded the presence of possible metal ions (e.g.,  $\text{Fe}^{2+}$ ,  $\text{Cu}^{2+}$ ,  $\text{Ni}^{2+}$ ,  $\text{Zn}^{2+}$ ) in P-TNTs and TNTs.

The morphology of the prepared samples was characterized by scanning electron microscopy (SEM, Quanta FEG 250) and transmission electron microscopy (TEM, Talos F200X). The crystalline structures were analyzed by X-ray diffraction (XRD, Rigaku D/max 2500) with Cu  $K\alpha$  radiation ( $\lambda = 0.154598 \text{ nm}$ ). X-ray photoelectron spectroscopy (XPS, ESCALAB 250Xi, Thermo Scientific) was acquired with a monochromatic Al  $K\alpha$  radiation source.

### 2.2 NORR tests

All electrochemical properties were evaluated at ambient temperature and pressure in a gas-tight H-type cell separated by an anion exchange membrane (Nafion 211) with 1-butyl-1-methylpyrrolidinium tris(pentafluoroethyl)trifluorophosphate ([C4mpyr][eFAP], 50 mL,  $0.1 \text{ mol}\cdot\text{L}^{-1}$ ) solution. The Nafion membrane was pretreated according to the procedure reported in our previous study. A catalyst ink with concentration of  $0.1 \text{ mg}\cdot\text{mL}^{-1}$  was loaded onto a carbon paper. The as-prepared electrodes, graphite rod, and saturated calomel electrode were used as working electrode, counter electrode, and reference electrode, respectively. In this study, all potentials were calibrated against the reversible hydrogen electrode (RHE) scale. For NORR, chronoamperometric analysis test was conducted in NO (99.99% purity) saturated IL-containing electrolyte (i.e., [C4mpyr][eFAP]/ $\text{H}_2\text{O}$  with a mass ratio of 97:3) and the electrolyte was purged with Ar for 30 min before the test. The NO gas flow rate was set to be 20 sccm.

## 3 Results and discussion

The synthesis procedure and morphology characterizations of the samples are presented in Fig. 1. Figure 1(a) (refer to the Experimental section for more details) depicts that TNTs (Figs. S1 and S2, cf. ESM) were first prepared by a modified hydrothermal process reported by Kasuga et al. [27]. Then, the obtained suspension was washed in acidic solution to remove impurities. Finally, the P dopant was introduced into the  $\text{TiO}_2$  lattice by pyrolysis at high temperature with the addition of

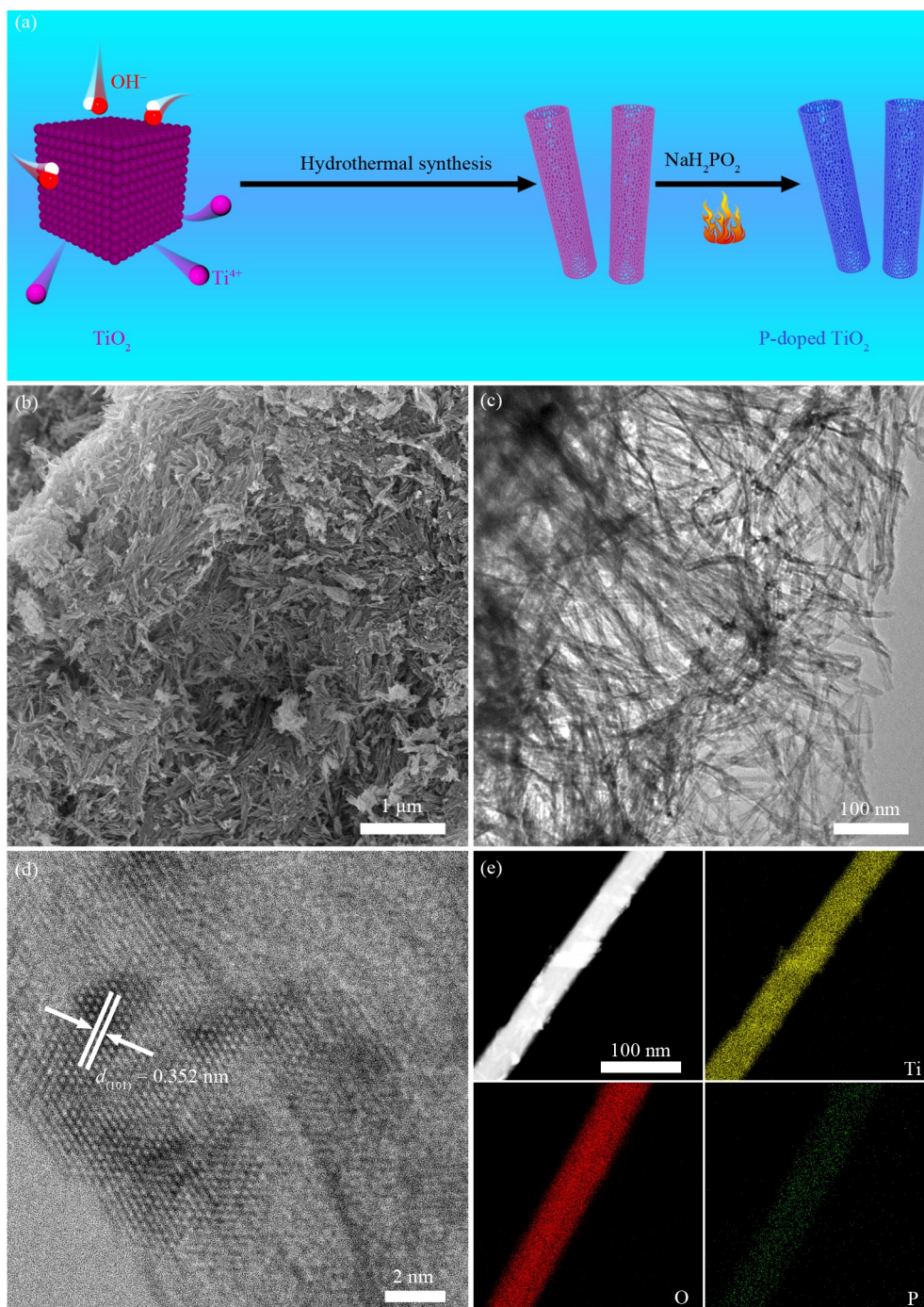


**Fig. 1** Synthesis and structural characterizations for P-TNTs: (a) synthetic depiction illustrating preparation of P-TNTs sample, (b) typical SEM images, and (c) TEM images of P-TNTs, (d) high-resolution TEM (HRTEM) image of P-TNTs, and (e) high-angle annular dark-field scanning TEM (HAADF-STEM) image and elemental mapping of Ti, O, and P in P-TNTs.

$\text{NaH}_2\text{PO}_4$  [28]. The SEM and TEM images were used to analyze these nanotubes. The results indicate that P-TNTs show a typical tube-like structure with a wall thickness in the range of 2–6 nm (Figs. 1(b, c)). Noteworthy, no obvious morphology change could be observed during the phosphorization.

Figure 1(d) exhibits the results of HRTEM characterization, showing the lattice fringes of P-TNTs with a  $d$ -spacing of 0.352 nm, which correspond to the (101)

crystal plane of anatase  $\text{TiO}_2$ . Additional HAADF-STEM and the corresponding EDX mapping images of P-TNTs indicate the P element is uniformly distributed throughout the TNTs (Fig. 1(e)).

The crystallographic structure of P-TNTs was characterized by XRD analysis (Fig. 2). Figure 2(a) demonstrates that all the characteristic peaks of P-TNTs match well with anatase phase  $\text{TiO}_2$  (JCPDS No. 21-1272). Moreover, no obvious peaks from other phases or impurities

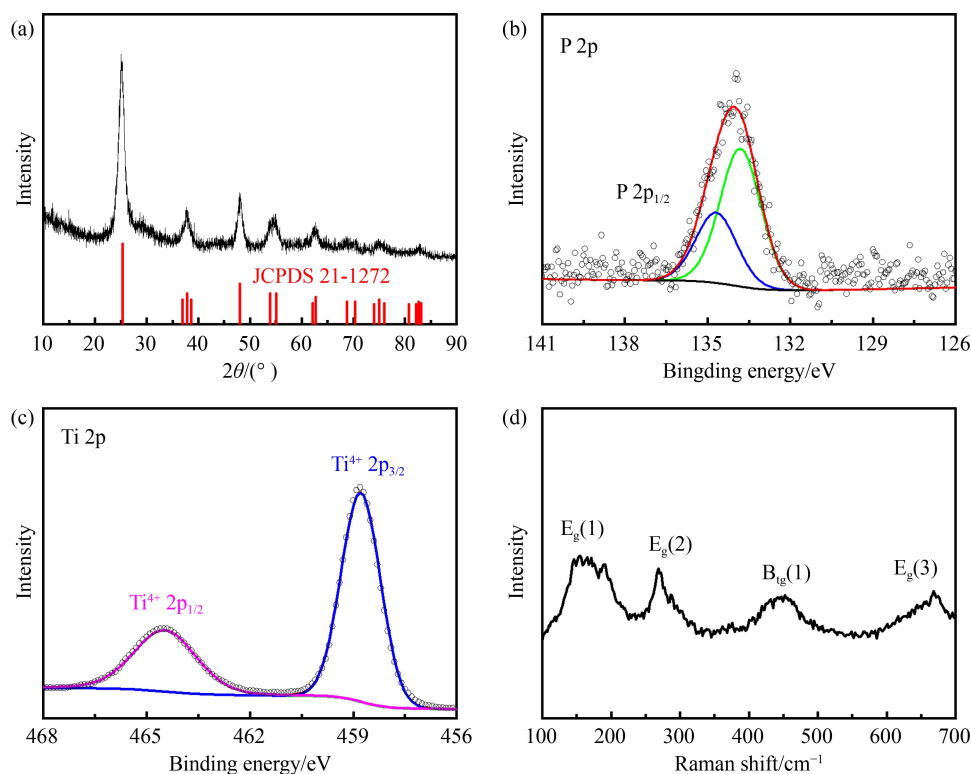


**Fig. 2** Fine structure of P-TNTs: (a) XRD pattern of P-TNTs, (b) and (c) high-resolution XPS spectra for P 2p and Ti 2p, and (d) Raman spectrum.

are observed. The surface compositions and electronic structures of P-TNTs were further characterized by XPS measurements. Figure S3 (cf. ESM) reveals that XPS survey spectrum confirms the existence of Ti, O, and P elements in these nanotubes. High-resolution P 2p XPS spectrum shows two peaks located at 134.3 and 133.4 eV, which can be assigned to P 2p<sub>1/2</sub> and P 2p<sub>3/2</sub> (corresponding to P–O–Ti), respectively (Fig. 2(b)) [28,29], confirming the successful doping of P in TNTs to form P-TNTs. Moreover, the P content in P-TNTs is 1.65 wt %, measured by ammonium molybdate spectrophotometry, which is close to that estimated from XPS measurement (1.58 wt %).

The XPS spectrum at Ti 2p region (Fig. 2(c)) shows two peaks at 464.5 and 458.8 eV corresponding to Ti<sup>4+</sup> oxidation state of P-TNTs. Besides, the comparison of Ti 2p XPS spectra shows a negative shift after the P doping (Fig. S4, cf. ESM), which can be explained from the larger charges on P (1.89) compared to that on Ti (1.34) [30], thus the charges get accumulated around the P atom and the Ti atom exhibits lower binding energy. Furthermore, the negative shift of binding energy also indicates the feasibility of the electron transfer between the P dopants and TiO<sub>2</sub> [31]. In the O 1s XPS spectrum (Fig. S5, cf. ESM), three peaks at 530.3, 531.6, and 532.5 eV are indexed to Ti–O, P–O–Ti, and O–P, respectively [32]. Raman spectrum shown in Fig. 2(d) was further acquired, which shows peaks of anatase TiO<sub>2</sub> at 157, 267, 451, and 670 cm<sup>-1</sup>. All these above-men-

tioned results support the successful doping of P into the TiO<sub>2</sub> lattice. Moreover, the projected density of states (PDOS) for TNTs and P-TNTs confirm the appearance of new states originating from the 3p orbitals of P atom (Fig. S6, cf. ESM). The simulated results obtained in this study and reported in previous studies indicate that P doping can effectively reduce the band gap of TiO<sub>2</sub> [29,33], and is significantly beneficial for faster charge transfer during the electrolysis.

Next, the NORR performances of P-TNTs and TNTs were evaluated and compared in a typical H-cell with three-electrode system in NO-saturated [C4mpyr][eFAP] (3 wt % water) solution (Fig. 3). The generated NH<sub>3</sub> was quantified by indophenol blue spectrophotometric method and carefully calibrated (Fig. S7, cf. ESM). Herein, all reported potentials were obtained versus the RHE. Figure S8 (cf. ESM) displays that the polarization curve of P-TNTs shows an increased current density compared with the polarization curve recorded under Ar-saturated electrolyte, indicating that P-TNTs sample is active toward NORR. Moreover, P-TNTs deliver larger current densities compared with TNTs (Fig. 3(a)), manifesting the beneficial role of P dopant in the TiO<sub>2</sub> lattice. Notably, prior to NORR, the current density is less than 1 mA·cm<sup>-2</sup> in the potential range from 0.1 to -0.8 V vs RHE. Further, the NORR activity of the two samples under different working potentials was investigated herein. Figure 3(b) illustrates that the highest *FE*<sub>NH<sub>3</sub></sub> on TNTs is only 42% at -0.7 V vs RHE, while P-TNTs show

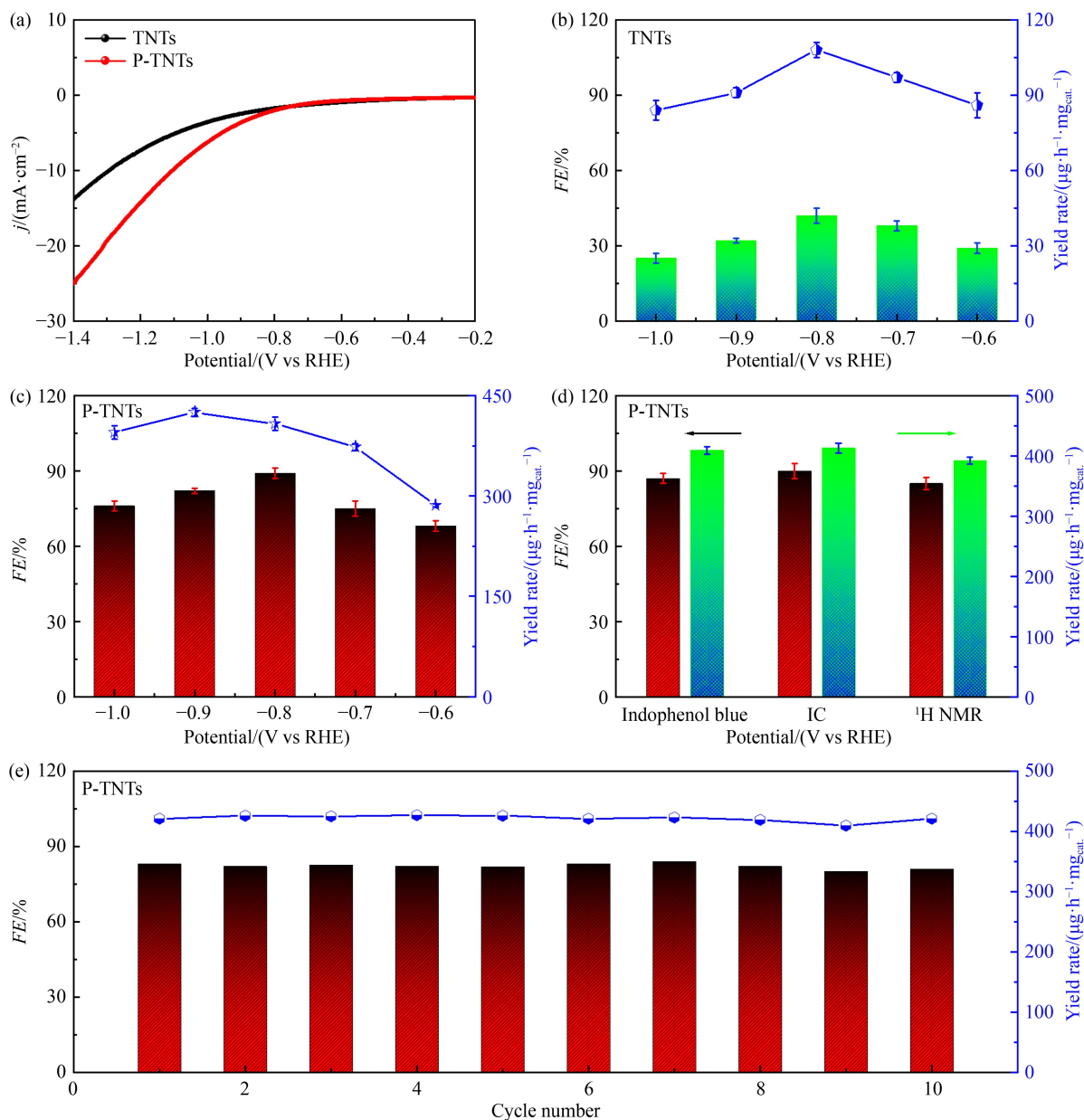


**Fig. 3** NORR performance of P-TNTs in an IL-containing electrolyte: (a) Polarization curves of TNTs and P-TNTs in NO-saturated electrolyte, supported on carbon paper, (b, c)  $FE_{NH_3}$  and yield rate at different applied potentials for TNTs and P-TNTs, respectively, (d)  $FE_{NH_3}$  and yield rate of P-TNTs at  $-0.8$  V vs RHE detected by three independent quantification methods, (e)  $FE_{NH_3}$  and yield rate of P-TNTs during 10 consecutive recycling electrolysis. Error bars depicted in (b–d) represent the standard deviation of three independent samples.

two times higher  $FE_{NH_3}$  of 89% at  $-0.8$  V vs RHE (Fig. 3(c)). In contrast, the obtained maximal  $NH_3$  yield rate on P-TNTs is found to be  $425 \mu\text{g}\cdot\text{h}^{-1}\cdot\text{mg}_{\text{cat.}}^{-1}$ , significantly larger than that of TNTs (Figs. 3(b,c)). To verify the reliability of our spectrophotometric method, the  $FE_{NH_3}$  and yield rate of P-TNTs were further examined by <sup>1</sup>H nuclear magnetic resonance (<sup>1</sup>H NMR) and IC measurements (Fig. 3(d)), both of which give results very close to those quantified by indophenol blue method.

Surprisingly, the achieved  $FE_{NH_3}$  values for P-TNTs at more negative potentials still remain above 76% (Fig.

3(c)). This is mainly due to the utilization of IL-containing electrolyte that can effectively suppress the side reaction of HER [26], as confirmed by the NORR performance evaluated in aqueous solution (Fig. S9, cf. ESM). As expected, the  $FE_{NH_3}$  and yield rate values from aqueous electrolyte are all significantly lower than those from no-aqueous one. Remarkably, the obtained performance metrics of P-TNTs are comparable to the recently best-reported NORR results and outperform most of NRR catalysts (Table S1).

In order to prove the production of  $NH_3$  from NORR

process catalyzed by P-TNTs, additional control experiments were performed. Figure S10 (cf. ESM) exhibits that no  $\text{NH}_3$  was detected on P-TNTs when NO was replaced with Ar.  $^1\text{H}$  NMR spectrum also confirms this result (Fig. S11, cf. ESM). The two control experiments also excluded the possible nitrogen contaminate from the used [C4mpyr][eFAP]. Besides, no  $\text{NH}_3$  could be observed when NO was electrolyzed by P-TNTs at open circuit (Fig. S10). These results collectively confirm that the produced  $\text{NH}_3$  was derived from the NORR electrolysis on P-TNTs.

To explore the stability of P-TNTs, cycling test at  $-0.8$  V vs RHE was conducted (Fig. 3(e)). Clearly, no obvious fluctuations in  $FE_{\text{NH}_3}$  and corresponding yield rate could be found after 10 consecutive cycles, indicating the excellent electrochemical stability of P-TNTs. The stable NORR activity was also manifested by chronoamperometry measurements, where acceptable current density and yield rate changes were observed after the 30-h electrolysis (Fig. S12, cf. ESM). Additional XRD pattern and TEM image confirm the structural and morphological stability of P-TNTs (Figs. S13 and S14, cf. ESM).

Strikingly, the above-mentioned enhanced NORR activity of P-TNTs could be ascribed to the introduction of P dopants and unique tube-like structure, which were found to be beneficial for the exposure of more catalytically active sites and faster mass and charge transfer (Fig. 4). To verify this perspective, the double-

layer capacitance ( $C_{\text{dl}}$ ) of P-TNTs and TNTs was measured in this study. Figure 4(a) demonstrates that P-TNTs sample exhibits a larger  $C_{\text{dl}}$  value ( $31.7 \text{ mF}\cdot\text{cm}^{-2}$ ) than the counterpart ( $24.6 \text{ mF}\cdot\text{cm}^{-2}$ ), confirming that the P-doping resulted in an increased number of active sites for NORR [34,35]. Electrochemical impedance spectroscopy (EIS) measurements were performed, and the results presented in Fig. 4(b) manifest that P-TNTs sample possesses a smaller interfacial charge-transfer resistance ( $17.5 \Omega$ ) compared with TNTs ( $25.8 \Omega$ ), indicating a faster mass and charge transfer kinetics [36,37].

To reveal mechanistic insight into the intrinsic activity of P-TNTs, DFT calculations were carried out in this study. It is generally suggested that the HER competes with NORR [11], which usually induces a poor selectivity for  $\text{NH}_3$  production. Herein, the free energy profiles of hydrogen adsorption on the two catalysts were first calculated. The results indicate that P-TNTs sample shows a bit larger free-energy change for  $^*\text{H}$  adsorption ( $\Delta G_{\text{H}^*} = -0.39 \text{ eV}$ ) than that of TNTs ( $\Delta G_{\text{H}^*} = -0.42 \text{ eV}$ ). This result confirms that HER on P-TNTs is reinforced, to some degree (Fig. S15, cf. ESM). However, noteworthy, the usage of hydrophobic [C4mpyr][eFAP] could largely inhibit the competitive HER [38–41], as confirmed by the above-mentioned results (Figs. 3 and S7).

Figure S16 (cf. ESM) presents the differential charge density analysis, revealing that P-TNTs exhibited a substantial charge exchange with  $^*\text{NO}$ , thereby activating

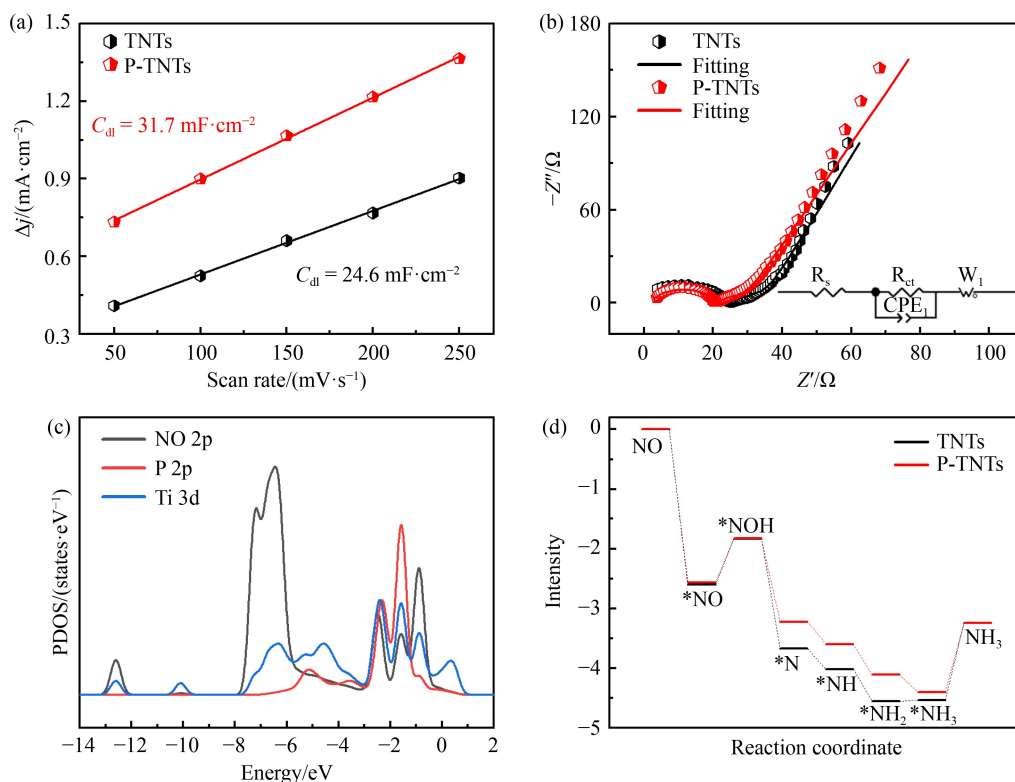


**Fig. 4** Experiments and theoretical simulations: (a) charging current density differences plotted against scan rates and (b) EIS spectra. The inset shows the equivalent circuit. (c) Calculated PDOS of P-TNTs and the adsorbed NO, corrected with Fermi level, and (d) calculated free energy diagrams of NORR.

adsorbed NO molecule by weakening the N–O bond (change from 1.163 Å to 1.311 Å). Besides, the PDOS for P-TNTs shown in Fig. 4(c) confirm the strong overlap of Ti 3d and P 2p valence orbitals with N 2p orbital, indicating that P-TNTs could effectively activate the NO molecule [42–44], which is in accordance with the analyses shown in Fig. S16.

Next, the free energy profiles of NORR catalyzed by P-TNTs and TNTs were obtained, as displayed in Fig. 4(d). The results indicate that the initial hydrogenation of P-TNTs was more energetically favorable, thus confirming a smaller energy barrier of 0.72 eV compared to TNTs (0.77 eV). Notably, the subsequent hydrogenation steps indicate downhill reaction processes. The largest reaction barrier occurs at the final desorption of \*NH<sub>3</sub>, as depicted in Fig. 4(d), where P-TNTs shows an energy barrier of 1.16 eV, obviously lower than that of TNTs (1.29 eV), indicating that P dopant can indeed significantly facilitate the NO-to-NH<sub>3</sub> conversion [45–50]. Overall, the strong affinity of NO molecule and decreased free-energy barriers induced by P doping synergistically optimize the NORR reaction paths.

### 3 Conclusions

In this study, P-doped TiO<sub>2</sub> nanotubes were successfully prepared for NH<sub>3</sub> production in IL-based electrolyte. The maximum  $FE_{\text{NH}_3}$  and yield rate could reach 89% (–0.8 V vs RHE) and 425 μg·h<sup>–1</sup>·mg<sub>cat</sub><sup>–1</sup> (–0.9 V vs RHE), respectively, both of which are comparable to the best-reported NORR electrocatalysts and outperform most of the NRR results. The remarkable improvement of NORR performance is ascribed to (1) the optimized electronic structure of TiO<sub>2</sub> induced by P doping, thereby activating NO molecule and reducing the energy barrier for the desorption of \*NH<sub>3</sub>, and (2) the employment of IL that efficiently suppresses the competitive HER. Therefore, this study offers a promising exploration for the development of high-performance electrocatalytic system for NH<sub>3</sub> synthesis by catalyst-electrolyte engineering strategy.

**Acknowledgements** This work was financially supported by the National Natural Science Foundation of China (Grant Nos. 22075211, 21601136, and 21905246) and the Key Projects of Zhejiang Natural Science Foundation (Grant No. LZ20E010001).

**Electronic Supplementary Material** Supplementary material is available in the online version of this article at <https://dx.doi.org/10.1007/s11705-022-2274-8> and is accessible for authorized users.

### References

1. Gruber N, Galloway J N. An earth-system perspective of the

global nitrogen cycle. *Nature*, 2008, 451(7176): 293–296

- Liang J, Liu Q, Alshehri A, Sun X. Recent advances in nanostructured heterogeneous catalysts for N-cycle electrocatalysis. *Nano Research Energy*, 2022, 1: e9120010
- Siddharth K, Wang Y, Wang J, Xiao F, Nambafu G, Shahid U, Yang F, Delmo E, Shao M. Platinum on nitrogen doped graphene and tungsten carbide supports for ammonia electro-oxidation reaction. *Frontiers of Chemical Science and Engineering*, 2022, 16(6): 930–938
- Dai Y, Xiong Y. Control of selectivity in organic synthesis via heterogeneous photocatalysis under visible light. *Nano Research Energy*, 2022, 1: e9120006
- Xu C, Huang J, Ma J. Green, cheap and rechargeable Al-N<sub>2</sub> battery with efficient N<sub>2</sub> fixation. *Rare Metals*, 2021, 40(1): 1–2
- Liu Y, Wang J, Zhang J, Qi T, Chu G, Zou H, Sun B. NO<sub>x</sub> removal by non-thermal plasma reduction: experimental and theoretical investigations. *Frontiers of Chemical Science and Engineering*, 2022, 16(10): 1476–1484
- Cao N, Chen Z, Zang K, Xu J, Zhong J, Luo J, Xu X, Zheng G. Doping strain induced bi-Ti<sup>3+</sup> pairs for efficient N<sub>2</sub> activation and electrocatalytic fixation. *Nature Communications*, 2019, 10(1): 2877
- Bao D, Zhang Q, Meng F L, Zhong H X, Shi M M, Zhang Y, Yan J M, Jiang Q, Zhang X B. Electrochemical reduction of N<sub>2</sub> under ambient conditions for artificial N<sub>2</sub> fixation and renewable energy storage using N<sub>2</sub>/NH<sub>3</sub> cycle. *Advanced Materials*, 2017, 29(3): 1604799
- Xu T, Liang J, Yue L, Liu Q, Li T, Zhao H, Luo Y, Lu S, Sun X. Recent progress in metal-free electrocatalysts toward ambient N<sub>2</sub> reduction reaction. *Acta Physico-Chimica Sinica*, 2021, 37(7): 2009043 (in Chinese)
- Wang J, Ding W, Wei Z. Performance of polymer electrolyte membrane fuel cells at ultra-low platinum loadings. *Acta Physico-Chimica Sinica*, 2021, 37(9): 2009094 (in Chinese)
- Long J, Chen S, Zhang Y, Guo C, Fu X, Deng D, Xiao J. Direct electrochemical ammonia synthesis from nitric oxide. *Angewandte Chemie International Edition*, 2020, 59(24): 9711–9718
- Peng X, Mi Y, Bao H, Liu Y, Qi D, Qiu Y, Zhuo L, Zhao S, Sun J, Tang X, Luo J, Liu X. Ambient electrosynthesis of ammonia with efficient denitration. *Nano Energy*, 2020, 78: 105321
- Yao Y, Wang J, Shahid U B, Gu M, Wang H, Li H, Shao M. Electrochemical synthesis of ammonia from nitrogen under mild conditions: current status and challenges. *Electrochemical Energy Reviews*, 2020, 3(2): 239–270
- Chen J, Zhang W, Li H, Li W, Zhao D. Recent advances in TiO<sub>2</sub>-based catalysts for N<sub>2</sub> reduction reaction. *Sustainable Materials*, 2021, 1(2): 174–193
- Hong Q, Li T, Zheng S, Chen H, Chu H, Xu K, Li S, Mei Z, Zhao Q, Ren W, Zhao W-G, Pan F. Tuning double layer structure of WO<sub>3</sub> nanobelt for promoting the electrochemical nitrogen reduction reaction in water. *Chinese Journal of Structural Chemistry*, 2021, 40(4): 519–526
- Kong Y, Li Y, Sang X, Yang B, Li Z, Zheng S, Zhang Q, Yao S, Yang X, Lei L, Zhou S, Wu G, Hou Y. Atomically dispersed zinc(I) active sites to accelerate nitrogen reduction kinetics for

- ammonia electrosynthesis. *Advanced Materials*, 2022, 34(2): 2103548
17. Li Y, Li J, Huang J, Chen J, Kong Y, Yang B, Li Z, Lei L, Chai G, Wen Z, Dai L, Hou Y. Boosting electroreduction kinetics of nitrogen to ammonia via tuning electron distribution of single-atomic iron sites. *Angewandte Chemie International Edition*, 2021, 60(16): 9078–9085
  18. Manjunatha R, Karajić A, Liu M, Zhai Z, Dong L, Yan W, Wilkinson D P, Zhang J. A review of composite/hybrid electrocatalysts and photocatalysts for Nitrogen reduction reactions: advanced materials, mechanisms, challenges and perspectives. *Electrochemical Energy Reviews*, 2020, 3(3): 506–540
  19. Liang J, Liu P, Li Q, Li T, Yue L, Luo Y, Liu Q, Li N, Tang B, Alshehri A, Shakir I, Agboola P O, Sun C, Sun X. Amorphous boron carbide on titanium dioxide nanobelt arrays for high-efficiency electrocatalytic NO reduction to NH<sub>3</sub>. *Angewandte Chemie International Edition*, 2022, 61(18): e202202087
  20. Du L, Xing L, Zhang G, Liu X, Rawach D, Sun S. Engineering of electrocatalyst/electrolyte interface for ambient ammonia synthesis. *SusMat*, 2021, 1(2): 150–173
  21. Zhang L, Liang J, Wang Y, Mou T, Lin Y, Yue L, Li T, Liu Q, Luo Y, Li N, Tang B, Liu Y, Gao S, Alshehri A A, Guo X, Ma D, Sun X. High-performance electrochemical NO reduction into NH<sub>3</sub> by MoS<sub>2</sub> nanosheet. *Angewandte Chemie International Edition*, 2021, 60(48): 25263–25268
  22. Hou J, Peng X, Sun J, Zhang S, Liu Q, Wang X, Luo J, Liu X. Accelerating hydrazine-assisted hydrogen production kinetics with Mn dopant modulated CoS<sub>2</sub> nanowire arrays. *Inorganic Chemistry Frontiers*, 2022, 9(12): 3047–3058
  23. Zhang F, Xie K. Porous iron- and cobalt-based single crystals with enhanced electrocatalysis performance. *Chinese Journal of Structural Chemistry*, 2021, 40(1): 61–69
  24. Wang X, Liu S, Zhang H, Zhang S, Meng G, Liu Q, Sun Z, Luo J, Liu X. Polycrystalline SnS<sub>x</sub> nanofilm enables CO<sub>2</sub> electroreduction to formate with high current density. *Chemical Communications*, 2022, 58(55): 7654–7657
  25. Wang G, Shen P, Luo Y, Li X, Li X, Chu K. A vacancy engineered MnO<sub>2-x</sub> electrocatalyst promotes nitrate electroreduction to ammonia. *Dalton Transactions*, 2022, 51(24): 9206–9212
  26. Luo Y, Li Q, Tian Y, Liu Y, Chu K. Amorphization engineered VSe<sub>2-x</sub> nanosheets with abundant Se-vacancies for enhanced N<sub>2</sub> electroreduction. *Journal of Materials Chemistry A: Materials for Energy and Sustainability*, 2022, 10(4): 1742–1749
  27. Kasuga T, Hiramatsu M, Hoson A, Sekino T, Niihara K. Titania nanotubes prepared by chemical processing. *Advanced Materials*, 1999, 11(15): 1307–1311
  28. Zhao X, Zhuo D, Chen Q, Guo G. Enhancing electrochemical reduction of CO<sub>2</sub> to formate by regulating the support morphology. *Chinese Journal of Structural Chemistry*, 2021, 40(3): 376–382
  29. Liu D, Li H, Gao R, Zhao Q, Yang Z, Gao X, Wang Z, Zhang F, Wu W. Enhanced visible light photoelectrocatalytic degradation of tetracycline hydrochloride by I and P co-doped TiO<sub>2</sub> photoelectrode. *Journal of Hazardous Materials*, 2021, 406: 124309
  30. Wei Z, Wang J, Guo S, Tan S. Towards highly salt-rejecting solar interfacial evaporation: photothermal materials selection, structural designs, and energy management. *Nano Research Energy*, 2022, 1: e9120014
  31. Wang K, Yu J, Liu L, Hou L, Jin F. Hierarchical P-doped TiO<sub>2</sub> nanotubes array@Ti plate: towards advanced CO<sub>2</sub> photocatalytic reduction catalysts. *Ceramics International*, 2016, 42(14): 16405–16411
  32. Guan Z, Zou K, Wang X, Deng Y, Chen G. The synergistic effect of P-doping and carbon coating for boosting electrochemical performance of TiO<sub>2</sub> nanospheres for sodium-ion batteries. *Chinese Chemical Letters*, 2021, 32(12): 3847–3851
  33. Meng L, Li L. Recent research progress on operational stability of metal oxide/sulfide photoanodes in photoelectrochemical cells. *Nano Research Energy*, 2022, 1: e9120020
  34. Liu D, Zeng Q, Hu C, Chen D, Liu H, Han Y, Xu L, Zhang Q, Yang J. Light doping of tungsten into copper-platinum nanoalloys for boosting their electrocatalytic performance in methanol oxidation. *Nano Research Energy*, 2022, 1: e9120017
  35. Liu S, Jin M, Sun J, Qin Y, Gao S, Chen Y, Zhang S, Luo J, Liu X. Coordination environment engineering to boost electrocatalytic CO<sub>2</sub> reduction performance by introducing boron into single-Fe-atomic catalyst. *Chemical Engineering Journal*, 2022, 437: 437
  36. Zhang S, Gao X T, Hou P F, Zhang T R, Kang P. Nitrogen-doped Zn-Ni oxide for electrochemical reduction of carbon dioxide in sea water. *Rare Metals*, 2021, 40(11): 3117–3124
  37. Gao X, Li J, Zuo Z. Advanced electrochemical energy storage and conversion on graphdiyne interface. *Nano Research Energy*, 2022, 1: e9120036
  38. Seyedhosein P, Florian S, Andrey M, Aleksandr K, Torsten B. Tailoring the LiNbO<sub>3</sub> coating of Ni-rich cathode materials for stable and high-performance all-solid-state batteries. *Nano Research Energy*, 2022, 1: e9120016
  39. Meng G, Wei T, Liu W, Li W, Zhang S, Liu W, Liu Q, Bao H, Luo J, Liu X. NiFe layered double hydroxide nanosheet array for high-efficiency electrocatalytic reduction of nitric oxide to ammonia. *Chemical Communications*, 2022, 58(58): 8097–8100
  40. Qi D, Lv F, Wei T, Jin M, Meng G, Zhang S, Liu Q, Liu W, Ma D, Hamdy M S, Luo J, Liu X. High-efficiency electrocatalytic NO reduction to NH<sub>3</sub> by nanoporous VN. *Nano Research Energy*, 2022, 1: e9120022
  41. Li L, Hasan I, Farwa, He R, Peng L, Xu N, Niazi N, Zhang J, Qiao J. Copper as a single metal atom based photo-, electro- and photoelectrochemical catalyst decorated on carbon nitride surface for efficient CO<sub>2</sub> reduction: a review. *Nano Research Energy*, 2022, 1: e9120015
  42. Meng G, Jin M, Wei T, Liu Q, Zhang S, Peng X, Luo J, Liu X. MoC nanocrystals confined in N-doped carbon nanosheets toward highly selective electrocatalytic nitric oxide reduction to ammonia. *Nano Research*, 2022, 15(10): 8890–8896
  43. Zhang H, Luo Y, Chu P K, Liu Q, Liu X, Zhang S, Luo J, Wang X, Hu G. Recent advances in non-noble metal-based bifunctional electrocatalysts for overall seawater splitting. *Journal of Alloys and Compounds*, 2022, 922: 166113

44. Ding J, Yang H, Zhang S, Liu Q, Cao H, Luo J, Liu X. Advances in electrocatalytic hydrogen evolution reaction by metal nanoclusters-based materials. *Small*, 2022, 18(52): 2204524
45. Wang Z, Pu Y, Wang D, Wang J X, Chen J F. Recent advances on metal-free graphene-based catalysts for the production of industrial chemicals. *Frontiers of Chemical Science and Engineering*, 2018, 12(4): 855–866
46. Jiang L, Dong D, Lu Y. Design strategies for low temperature aqueous electrolytes. *Nano Research Energy*, 2022, 1: e9120003
47. Reverberi A P, Varbanov P S, Vocciante M, Fabiano B. Bismuth oxide-related photocatalysts in green nanotechnology: a critical analysis. *Frontiers of Chemical Science and Engineering*, 2018, 12(4): 878–892
48. Liu W, Feng J, Wei T, Liu Q, Zhang S, Luo Y, Luo J, Liu X. Active-site and interface engineering of cathode materials for aqueous Zn-gas batteries. *Nano Research*, 2022, in press
49. Guo F, Zhang M, Yi S, Li X, Xin R, Yang M, Liu B, Chen H, Li H, Liu Y. Metal-coordinated porous polydopamine nanospheres derived Fe<sub>3</sub>N-FeCo encapsulated N-doped carbon as a highly efficient electrocatalyst for oxygen reduction reaction. *Nano Research Energy*, 2022, 1: e9120027
50. Zhang K, Liang X, Wang L, Sun K, Wang Y, Xie Z, Wu Q, Bai X, Hamdy M, Chen H, Zou X. Status and perspectives of key materials for PEM electrolyzer. *Nano Research Energy*, 2022, 1: e9120032